

Ellipse Recovery from Blurred Binary Images

Hojatollah Zamani, *Student Member, IEEE*, Arash Amini, *Senior Member, IEEE*

Abstract—In this paper, we address the problem of ellipse recovery from blurred shape images. A shape image is a binary-valued (0/1) image in continuous-domain that represents one or multiple shapes. In general, the shapes can also be overlapping. We assume to observe the shape image through finitely many blurred samples, where the 2D blurring kernel is assumed to be known. The samples might also be noisy. Our goal is to detect and locate ellipses within the shape image. Our approach is based on representing an ellipse as the zero-level-set of a bivariate polynomial of degree 2. Indeed, similar to the theory of finite rate of innovation (FRI), we establish a set of linear equations (annihilation filter) between the image moments and the coefficients of the bivariate polynomial. For a single ellipse, we show that the image can be perfectly recovered from only 6 image moments (improving the bound in [1]). For multiple ellipses, instead of searching for a polynomial of higher degree, we locally search for single ellipses and apply a pooling technique to detect the ellipse. As we always search for a polynomial of degree 2, this approach is more robust against additive noise compared to the strategy of searching for a polynomial of higher degree (detecting multiple ellipses at the same time). Besides, this approach has the advantage of detecting ellipses even when they intersect and some parts of the boundaries are lost. Simulation results using both synthetic and real world images (red blood cells) confirm superiority of the performance of the proposed method against the existing techniques.

Index Terms—Algebraic curves, blurred images, ellipse recovery, finite rate of innovation, image moments.

I. INTRODUCTION

THE ellipse recovery from digital pixels is a well-studied task in computer vision [2], pattern recognition [3] and has various applications in astronomy [4], biomedical imaging [5]–[8], process control in semiconductor industry [9], traffic sign detection [10], object tracking [11], and pupil detection [12].

An image that consists of ellipse-shaped objects is a continuous-domain signal which is mapped to a discrete-domain space via an imaging device. The optical part in most existing imaging devices can be fairly approximated with a linear and shift-invariant operator (a filter). This implies that the incoming light to the camera (the imaging device) is first convolved with a 2D blurring kernel, which is commonly referred to as the point spread function (PSF). Next, the blurred image is sampled to form the output samples. As the boundary of an ellipse in the discrete-domain image is affected by both the PSF and the sampling process, detecting and locating the ellipse based on the pixels is no longer an easy task. In particular, note that the width of the boundary is not necessarily limited to one pixel (depending on the PSF) and simple curve fitting techniques are not sufficient to locate

the ellipse. Another issue is that the sampling process might introduce some noise in the pixels; thus, a practical ellipse detection method shall also be robust to additive noise.

A. Related works

There is a rich literature on ellipse detection over the past three decades and various methods are proposed. All introduced methods are based on unique properties of the ellipse. The two main categories of more successful methods are clustering or voting techniques based on Hough transform (HT) and algebraic/geometric least square (LS) techniques.

The Hough transform is a voting scheme that assigns a confidence value to each possible ellipse in the image. A thresholding operator then, determines the most likely ellipses. The HT-based methods are known to be robust against outliers; in addition, HT allows for detection of multiple ellipses at the same time. However, the HT-based methods usually have high computational complexity and their storage requirement scales exponentially in terms of the number of involved parameters [13]. Several simplifications are introduced in [14], [15] to overcome these issues. One of the efficient HT-based methods is presented in [16]; in our numerical comparisons, we include this method as a representative of the HT-based methods.

The LS-based algorithms use a parametric representation of the ellipse and try to estimate the parameters by minimizing a quadratic cost (e.g., the distance between the data points and the ellipse curve); based on the definition of the cost, the method is classified as algebraic or geometric. In algebraic LS-based methods, a parametric algebraic expression is assumed between the x and y coordinates of the ellipse boundary points. Therefore, each known boundary point on the ellipse provides us with an equation involving the parameters. This shows that the parameters are the solution of a set of equations established by the known boundary points.

Bookstein [17] showed that under a quadratic constraint, the problem can be modeled as a generalized eigenvector problem with a closed-form solution. Direct least squares (DLS) algorithm with equality constraint was first proposed by Fitzgibbon [18]. Thanks to simplicity and non-iterative property of DLS, this algorithm is widely used in real world applications. However, as studied in [19], the matrices involved in DLS are sometimes singular; to avoid numerical instability, a matrix decomposing technique is proposed in [19].

If the available boundary points cover only part of the ellipse, the algebraic methods are likely to estimate a smaller shape. To overcome this issue, geometric LS-based methods fit an ellipse to the data so as to minimize the orthogonal distance of the available points to the boundary of the estimated shape [20], [21]. Unlike algebraic methods, the geometric techniques are commonly iterative and do not have closed-form solutions.

Authors are with the EE Department of Sharif University of Technology, Tehran, Iran (e-mail: hojatollah.zamani@ee.sharif.edu, aamini@sharif.edu). This work is supported by Iran National Science Foundation (INSF).

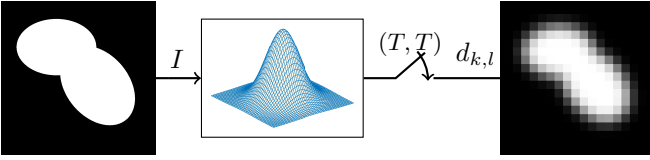


Fig. 1. The imaging system. The input image convolved with 2D kernel and afterward the uniform sampling applied to generate the measurements.

A recent approach used in binary images is the framework of signals with finite rate of innovation (FRI). In this framework, which was first developed for 1D signals in [22] (and extended to 2D in [23]), a family of signals with certain piece-wise structures are studied, where each piece can be represented with finitely many parameters. The structures are linked with a set of algebraic equations referred to as the annihilation filters. Well-known examples include the stream of Diracs and piece-wise polynomial signals. Specifically, a non-iterative ellipse fitting method based on the tools in FRI theory is developed in [24]. The ellipse detection is a special case of shape recovery, which is considered in more generality within the 2D FRI framework. The recovery of piece-wise continuous complex analytic images proposed in [25] is an example of the FRI framework in 2D where the complex derivative of such images is the zero-level-set of a polynomial associated with periodic band-limited functions.

The application of the FRI theory in recovering binary image shapes is studied in [1], [26]. By modeling the boundary of image shapes using algebraic curves, an annihilation-based recovery method is proposed in [1], which essentially recovers the derivative of the image. It is particularly shown that for the recovery of an algebraic curve of degree n (the degree of the polynomial that represents the shape), $3n - 1$ image moments are sufficient (the moments are evaluated based on pixel values). A similar problem is investigated in [27], where the image is recovered from the Fourier samples (rather than spatial pixels). Again, the guaranteed bound confirms with the $3n - 1$ moments in [1]. The latter bound is improved to $2n + 1$ moments in [28] for the case of convex algebraic curves.

Other than the general approaches mentioned above, there are some ellipse detection methods in the literature. For instance, a circle detection method (extendable to ellipses) using pairs of opposite boundary points is devised in [29]. An algorithm based on the local concavity of the edges is proposed in [5]. Techniques based on principal component analysis (PCA) and maximum likelihood are provided in [30] and [31], respectively. Another stochastic approach using the marked point process framework is presented in [32]. [33] introduced a fitting technique by taking advantage of the sparsity of the outliers. Among the recent deep learning approaches one can name [34]; although deep learning methods are potentially very accurate, their performances are greatly impacted by the employed training dataset.

B. Challenges in ellipse recovery

In this paper, we are interested in detecting multiple ellipses in a continuous-domain binary image like the one in left plot of Fig. 1. The imaging/measurement system transforms this

image into a finite number of pixels by convolving it with a 2D kernel (the PSF, shown in the middle plot) followed by a uniform sampling. Therefore, the resulting image in the right plot of Fig. 1 consists of blurred pixels. Now, the main challenge is to detect the number of existing ellipses in the image and to estimate their coefficients from the pixels. As we shall show in our simulations, the standard HT or LS-based methods fail as they ignore the blurring effect and try to fit an ellipse to the boundary points; due to the blurring effect, the exact location of ellipse boundaries cannot be determined from the pixels.

Another issue is when we have multiple ellipses in an image. Besides the fact that FRI-based methods (such as the one in [1]) need to know an upper-bound on the number of ellipses in advance, they become very sensitive to additive noise with the increase of the number of ellipses. The reason is the use of polynomial equations of high degrees.

The overlapping of the ellipses is also another challenge for almost all the existing methods. The blurred image of two overlapping ellipses could be easily mistaken with the image of a single but larger ellipse.

C. Contributions

In this paper, we study the problem of multiple ellipse recovery from blurred pixels by knowing the blurring kernel. Similar to the approach in [1], we represent each ellipse with the zero-level-set of a bivariate polynomial (algebraic curve) of degree 2; however, we locally search for the ellipses as opposed to higher order curves which has the advantage of restricting the degree to 2 irrespective of the number of ellipses. In each step, we derive a set of annihilation equations to estimate the coefficients of a degree 2 algebraic curve. To ensure that the estimated algebraic curve represents an ellipse we introduce a quadratic optimization problem. Moreover, we theoretically guarantee the uniqueness of the minimizer.

We further improve the theoretical bound for the required number of image moments to extract an ellipse. It is proven in [1] that for recovering a degree n algebraic curve, moments of degrees up to $3n - 1$ are sufficient; the image has $\binom{3n+1}{2}$ moments with this degree constraint. The latter bound is improved to moments of up to degree $2n + 1$ when the shape is known to be convex (which is the case for an ellipse). Interestingly, for the case of an ellipse with $n = 2$, these two bounds coincide and require moments of up to degree 5 (21 moments in total). We show in this paper that the moments of up to degree 2 (6 moments in total) are sufficient for the recovery of an ellipse. This forms a tight bound as an ellipse is parametrized using 6 coefficients.

As we would like to detect multiple ellipses which can potentially intersect (and overlap), we devise a patch-wise approach in which we search for an ellipse within a small window (the patch). This window can include only a part of an ellipse and our task is to estimate the parameters of an ellipse only by observing a fraction of its blurred boundary. Therefore, we introduce the generalized moments and modify the annihilation equations accordingly.

D. Paper organization

The rest of this paper is organized as follows: in Section II we describe the image model, the sampling operator, and the image recovery based on the moments. In Section III, we first elaborate on estimating the coefficients of a single ellipse using annihilation equations. We further present our theoretical results on the uniqueness of the solution and the sufficient degree of moments for perfect reconstruction. Next, we introduce our patch-based approach for the detection of multiple ellipses. The simulation results in Section IV confirm the efficiency and robustness of the introduced method both in the noiseless and noisy settings. Finally, we conclude the paper in Section V.

II. CONTINUOUS-DOMAIN IMAGE MODEL AND SAMPLING

In this section, we define our binary image model via algebraic curves and explain the imaging system. We also link the image recovery problem with the annihilation equations in the FRI terminology. This helps us in deriving a sampling theorem for images.

A. Shape images

A bivariate polynomial of degree n with real coefficients $a_{i,j}$ is denoted by

$$p(x, y) = \sum_{0 \leq i, j, i+j \leq n} a_{i,j} x^i y^j, \quad (1)$$

where x, y represent the real-valued input arguments. The algebraic domain corresponding to $p(x, y)$ is defined as the set of points $\{(x, y) \in \mathbb{R}^2 : p(x, y) \leq 0\}$. The boundary of this domain is the zero-level-set of $p(x, y)$ which is the algebraic curve of degree n . We define the continuous-domain binary algebraic shape \mathcal{S} associated with $p(x, y)$ as

$$\mathcal{S}_p(x, y) = \mathbb{1}_{p(x,y) \leq 0} \quad (x, y) \in \Omega, \quad (2)$$

where $\mathbb{1}$ is the indicator function, $\Omega = [-L, L]^2$, and integer $L \in \mathbb{Z}^+$ (which determines the boundary of the image) is assumed to be large enough.

The ellipses (which are of particular interest in this paper) are special cases of algebraic shapes of degree 2 polynomials. Note that the algebraic shape of a degree 2 polynomial is not necessarily an ellipse (e.g., parabolas and hyperbolas). The shape boundary of a binary image consisting of N ellipses (not necessarily a connected curve) is always included in the algebraic curve of a degree $2N$ polynomial; by multiplying the degree 2 polynomials associated with each ellipse, we obtain a degree $2N$ polynomial that vanishes on the boundary of each ellipse. However, note that if the ellipses are overlapping, some part of the ellipse boundaries can be excluded in the shape boundaries, while they appear in the corresponding algebraic curve. Another issue is that while the shape boundary of the original image can be represented by an algebraic curve, the image itself might not coincide with any algebraic shape (e.g., the left image in Fig. 1). The continuous-domain images in this paper are assumed to be binary (0/1-valued) such that the boundaries belong to a union of N ellipses, but the shape image is not necessarily assumed to be an algebraic shape.

B. Imaging system

The imaging device (or simply the camera) is the operator that maps the continuous-domain (binary) image into a finite set of pixels. To better explain the effect of this device, let $I(x, y)$ denote the input continuous-domain image and let us represent the output pixels by $\{d_{k,l}\}$ (k and l are integers). A naive camera model is a uniform 2D sampler, i.e., $d_{k,l} = I(kT, lT)$, where T is the spatial sampling resolution. This model is unrealistic due to the physical limitations of the imaging device. A more realistic model is

$$d_{k,l} = \frac{1}{T^2} \iint_{\Omega} I(x, y) \varphi\left(\frac{x}{T} - k, \frac{y}{T} - l\right) dx dy, \quad (3)$$

where $\varphi(x, y)$ is the sampling kernel or the point spread function of the camera. In general, the pixels $\{d_{k,l}\}$ can also be corrupted by additive noise. A high-level block diagram of the imaging device is shown in Fig. 1.

Our goal in this paper is to recover $I(x, y)$ by having access to pixel values $\{d_{k,l}\}$. We assume to know the sampling kernel φ in advance and assume that $I(x, y)$ belongs to the shape model described in Section II-A.

C. Image recovery using annihilation equations

Let $I(x, y)$ be a continuous-domain binary image whose boundaries belong to the algebraic curve of the bivariate polynomial $p(x, y) = \sum a_{i,j} x^i y^j$ of degree n . Due to the binary nature of $I(x, y)$, we know that $\frac{\partial}{\partial x} I(x, y)$ and $\frac{\partial}{\partial y} I(x, y)$ are 2D images that are zero except at the boundaries where we expect Dirac-type behavior. Besides, the polynomial $p(x, y)$ vanishes at the boundary of $I(x, y)$. Similar to the 1D equality $x \delta(x) \equiv 0$, where $\delta(\cdot)$ is the Dirac's delta distribution, we can write that [1]

$$p(x, y) \frac{\partial}{\partial x} I(x, y) \equiv 0, \quad (4a)$$

$$p(x, y) \frac{\partial}{\partial y} I(x, y) \equiv 0. \quad (4b)$$

It is interesting to mention that (4) remains valid irrespective of the white/black coloring of the shape interior; further, the edges in $I(x, y)$ could be a subset (and not all) of the zero-level-set of $p(x, y)$. By integrating equalities in (4), we have that

$$\iint_{\Omega} x^r y^s g(x, y) p(x, y) \frac{\partial}{\partial x} I(x, y) dx dy = 0, \quad (5a)$$

$$\iint_{\Omega} x^r y^s g(x, y) p(x, y) \frac{\partial}{\partial y} I(x, y) dx dy = 0. \quad (5b)$$

Using the adjoint property of the partial derivatives, we can rewrite (5) as

$$- \iint_{\Omega} \frac{\partial}{\partial x} (x^r y^s g(x, y) p(x, y)) I(x, y) dx dy = 0, \quad (6a)$$

$$- \iint_{\Omega} \frac{\partial}{\partial y} (x^r y^s g(x, y) p(x, y)) I(x, y) dx dy = 0, \quad (6b)$$

which can be translated into constraints of the form

$$\sum_{0 \leq i, j, i+j \leq n} ((i+r)M_{i+r-1, j+s}^{g(x,y)} + M_{i+r, j+s}^{g(x,y)}) a_{i,j} = 0, \quad (7a)$$

$$\sum_{0 \leq i, j, i+j \leq n} ((j+s)M_{i+r, j+s-1}^{g(x,y)} + M_{i+r, j+s}^{g(x,y)}) a_{i,j} = 0, \quad (7b)$$

on generalized image moments (see [1] for the details)

$$M_{i,j}^{g(x,y)} \triangleq \iint_{\Omega} x^i y^j g(x,y) I(x,y) dx dy. \quad (8)$$

$M_{i,j}^{g_x(x,y)}$ and $M_{i,j}^{g_y(x,y)}$ are Similarly defined by using the partial derivatives of g as the weight function. Here, $g(\cdot, \cdot)$ is an arbitrary weight function that could be tuned (with $g \equiv 1$ we arrive at the standard image moments) with partial derivatives as $g_x(\cdot, \cdot)$ and $g_y(\cdot, \cdot)$. Interestingly, (7) provides a set of linear equations (called annihilation equations) for finding the polynomial coefficients $a_{i,j}$ based on the generalized image moments $M_{i,j}^{g(x,y)}$, $M_{i,j}^{g_x(x,y)}$, and $M_{i,j}^{g_y(x,y)}$ (we shall explain how to derive the moments from the pixels). Using the matrix notations, we can write

$$\mathbf{M}\mathbf{a} = \mathbf{0}, \quad (9)$$

where \mathbf{M} is a matrix formed by generalized image moments, \mathbf{a} is the vector of polynomial coefficients, and $\mathbf{0}$ is an all-zero vector matching the size of \mathbf{a} . Note that any scalar multiple of \mathbf{a} such as $\mathbf{a}' = \alpha\mathbf{a}$ also satisfies (9). Therefore, we enforce $a_{0,0} = 1$ to avoid multiple solutions; as $p(x,y)$ and $\alpha p(x,y)$ produce the same algebraic curves, this convention does not affect the image recovery task.

It remains to describe how the generalized moments are evaluated based on pixel values. For this purpose, let $g(x,y)$ be a non-trivial and non-negative-valued function such that $x^i y^j g(x,y)$ and its partial derivatives for $0 \leq i, j \leq \mu$ can be written as the linear combination of shifts of the PSF with coefficients $\{\vartheta_{k_1, k_2}^{(i,j)}\}, \{\nu_{k_1, k_2}^{(i,j)}\}, \{v_{k_1, k_2}^{(i,j)}\}$, i.e.,

$$\begin{aligned} \forall i, j = 0, \dots, \mu, \exists \{ \vartheta_{k_1, k_2}^{(i,j)} \}, \{ \nu_{k_1, k_2}^{(i,j)} \}, \{ v_{k_1, k_2}^{(i,j)} \} : \\ \sum_{k_1, k_2 \in \mathbb{Z}} \vartheta_{k_1, k_2}^{(i,j)} \varphi(x - k_1, y - k_2) = x^i y^j g(x, y), \\ \sum_{k_1, k_2 \in \mathbb{Z}} \nu_{k_1, k_2}^{(i,j)} \varphi(x - k_1, y - k_2) = x^i y^j g_x(x, y), \\ \sum_{k_1, k_2 \in \mathbb{Z}} v_{k_1, k_2}^{(i,j)} \varphi(x - k_1, y - k_2) = x^i y^j g_y(x, y). \end{aligned} \quad (10)$$

The parameter μ is the maximum order of the generalized image moment required in our recovery method. Obviously, the set of constraints in (10) becomes more restricting as μ grows. For $g \equiv 1$, (10) is known as the polynomial reproducing property of $\varphi(\cdot, \cdot)$ and is of interest in wavelet theory (the Strang-Fix condition for determining the approximation order of the wavelet). The 2D B-spline functions are well-known examples that satisfy this condition [35], [36]. Here, we have the freedom of choosing $g(\cdot, \cdot)$; besides, in most practical cases, it is numerically sufficient that (10) holds approximately (and not necessarily exactly). For the robustness of the generalized moments to cropping, it is desirable to have decaying $g(\cdot, \cdot)$ functions; with this choice, the moments are automatically evaluated locally.

By assuming (10), we can now relate the generalized moments to pixel values:

$$\begin{aligned} M_{i,j}^{g(x,y)} &= \iint_{\Omega} x^i y^j g(x,y) I(x,y) dx dy \\ &= \iint_{\Omega} \left(\sum_{k_1, k_2 \in \mathbb{Z}} \vartheta_{k_1, k_2}^{(i,j)} \varphi(x - k_1, y - k_2) \right) I(x,y) dx dy \\ &= \sum_{k_1, k_2 \in \mathbb{Z}} \vartheta_{k_1, k_2}^{(i,j)} \iint_{\Omega} \varphi(x - k_1, y - k_2) I(x,y) dx dy \\ &= \sum_{k_1, k_2 \in \mathbb{Z}} \vartheta_{k_1, k_2}^{(i,j)} d_{k_1, k_2}. \end{aligned} \quad (11)$$

Similarly, we have that

$$M_{i,j}^{g_x(x,y)} = \sum_{k_1, k_2 \in \mathbb{Z}} \nu_{k_1, k_2}^{(i,j)} d_{k_1, k_2}, \quad (12a)$$

$$M_{i,j}^{g_y(x,y)} = \sum_{k_1, k_2 \in \mathbb{Z}} v_{k_1, k_2}^{(i,j)} d_{k_1, k_2}. \quad (12b)$$

In summary, finding a suitable $g(\cdot, \cdot)$ (in terms of $\varphi(\cdot, \cdot)$) is the key to transform the pixels into the generalized moments.

D. Recovery guarantee

The annihilation equations in (9) help us in recovering the polynomial coefficients, and ultimately, the shape image. An important issue here is the number of required equations in (9) (or alternatively, the number of required image moments) from which we can extract the original polynomial. For this purpose, we describe a useful result from [1]:

Theorem 1: Let I denote an algebraic shape of degree n defined on Ω without singular edges. Also let $M_{i,j}^{g(x,y)}$, $M_{i,j}^{g_x(x,y)}$ and $M_{i,j}^{g_y(x,y)}$ denote the generalized moments of I corresponding to a non-trivial and non-negative-valued weight function $g(\cdot, \cdot)$. If $\tilde{\mathbf{a}} = [\tilde{a}_{i,j}]_{i+j \leq n} \neq \mathbf{0}$ satisfies the annihilation equations (7) for all $0 \leq r, s, r + s \leq 2n - 1$, then, the zero-level-set of the following polynomial contains the boundaries of I .

$$\tilde{p}(x,y) = \sum_{0 \leq i, j, i+j \leq n} \tilde{a}_{i,j} x^i y^j \quad (13)$$

With $0 \leq r, s, r + s \leq 2n - 1$ in Theorem 1, one needs the generalized moments of degree up to $3n - 1$ which consist of $2 \binom{3n+1}{2}$ equations. Compared to the $\binom{n+2}{2}$ unknowns (number of coefficients), this number is very large (almost 18 times the number of unknowns when n is large). The $3n - 1$ bound on the moment order is further improved to $2n + 1$, given that the shape image is convex [28]; thus, a suitable matrix \mathbf{M} shall have an aspect ratio close to 8 (instead of 18). In this paper and for the particular case of ellipses ($n = 2$), we prove that the 6 equations provided by the moments of degree up to 2 are sufficient to retrieve all the coefficients.

III. MAIN RESULT

In this section, we first study how to recover a single ellipse from the image moments by solving an optimization problem. We further discuss the uniqueness of the solution and the sufficient number of moments for the exact recovery. Next, we

introduce a patch-wise algorithm in order to estimate multiple ellipses where they can possibly be intersecting with each other.

A. Single ellipse recovery from the moments

Consider the following degree 2 bivariate polynomial

$$p(x, y) = a_{00} + a_{01}y + a_{10}x + a_{02}y^2 + a_{11}xy + a_{20}x^2 = 0. \quad (14)$$

The zero-level-set of $p(x, y)$ can be either an empty set, a point, a line, an ellipse, a parabola or a hyperbola. The special case of ellipse happens when $a_{11}^2 - 4a_{20}a_{02} < 0$. Enforcing this inequality in recovery procedures is rather complicated. Instead, it is common to scale the coefficients such that the equality $4a_{20}a_{02} - a_{11}^2 = 1$ holds [18]. We should highlight that the zero-level-set of a scaled polynomial remains unchanged; hence, this scaling does not affect the recovery procedure in a negative manner. By representing the polynomial coefficients as a vector \mathbf{a} , this equality constraint can be described as

$$\mathbf{a}^T \underbrace{\begin{bmatrix} 0 & 0 & 0 & 0 & 0 & 0 \\ 0 & 0 & 0 & 0 & 0 & 0 \\ 0 & 0 & 0 & 0 & 0 & 0 \\ 0 & 0 & 0 & 0 & 0 & 2 \\ 0 & 0 & 0 & 0 & -1 & 0 \\ 0 & 0 & 0 & 2 & 0 & 0 \end{bmatrix}}_{\mathbf{C}} \mathbf{a} = 1. \quad (15)$$

We can now reformulate the ellipse coefficient recovery from image moments (\mathbf{M}) via the following optimization problem with a quadratic constraint

$$\min_{\mathbf{a}} \|\mathbf{M}\mathbf{a}\|^2 \quad \text{s.t.} \quad \mathbf{a}^T \mathbf{C}\mathbf{a} = 1. \quad (16)$$

It should be highlighted that the constraint

$$a_{00} \leq a_{20}a_{01}^2 - a_{10}a_{11}a_{01} + a_{02}a_{10}^2 \quad (17)$$

shall be checked to make sure that the area of the detected ellipse is non-negative; i.e., if the constraint in (17) is violated, then, the detected ellipse is ignored.

Theorem 2: If \mathbf{M} is full column-rank, then, (16) has a unique minimizer. This minimizer can be expressed as

$$\mathbf{a}_{\text{opt}} = \zeta \mathbf{Q}^{-1} \mathbf{v}_{\text{max}}, \quad (18)$$

where $\mathbf{Q} = \sqrt{\mathbf{M}^T \mathbf{M}}$, \mathbf{v}_{max} stands for the unit-norm eigenvector of $\mathbf{Q}^{-1} \mathbf{C} \mathbf{Q}^{-1}$ corresponding to the maximum eigenvalue, and

$$\zeta = \frac{1}{\sqrt{\mathbf{v}_{\text{max}}^T \mathbf{Q}^{-1} \mathbf{C} \mathbf{Q}^{-1} \mathbf{v}_{\text{max}}}}. \quad (19)$$

Proof: See Appendix A.

Theorem 2 describes the solution and uniqueness of the minimization problem in (16). It does not, however, guarantee that if \mathbf{M} corresponds to the moments of an ellipse, the minimizer \mathbf{a}_{opt} coincides with the coefficients of this shape. From [1], we know that if we have enough moments (i.e., \mathbf{M} is tall enough), \mathbf{a}_{opt} exactly describes the ellipse. In Theorem 3, we improve the bound in [1] for the case of a single ellipse.

Theorem 3: Let $M_{i,j}^{g(x,y)}$, $M_{i,j}^{g_x(x,y)}$ and $M_{i,j}^{g_y(x,y)}$ denote the generalized moments of an ellipse \mathcal{S} , where $g(\cdot, \cdot)$ has a non-trivial and non-negative-valued weight function. Further, let

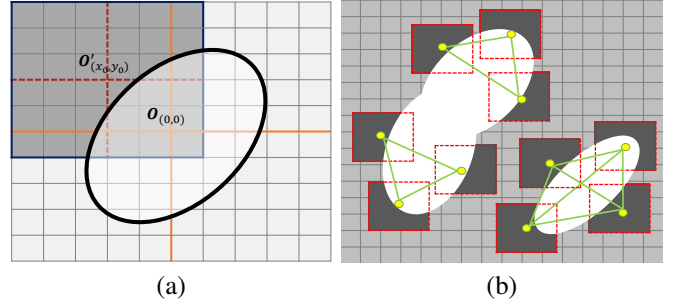


Fig. 2. (a) Estimating the coefficients of an ellipse from a window of samples using generalized moments. The coordinate of each window is different. We should compensate the shifted coordinate to describe on system (b) The fidelity metric of patches belong an ellipse are regenerated by a new patch of same ellipse.

$\tilde{\mathbf{a}} = [\tilde{a}_{i,j}]_{i+j \leq 2}$ be a non-trivial solution to (16) for $n = 2$ and $0 \leq r, s$ with $r+s \leq M_{\text{max}}$, that forms a non-zero polynomial $\tilde{p}(x, y) = \sum_{i,j} \tilde{a}_{i,j} x^i y^j$. Then,

- the zero-level-set of \tilde{p} coincides with the ellipse \mathcal{S} , given that $M_{\text{max}} = 3$, g is compact-support, and a part of the ellipse border is contained in the support of g (the choice of $M_{\text{max}} = 3$ translates into having moments of degree up to 5).
- the zero-level-set of \tilde{p} coincides with the ellipse \mathcal{S} , given that $M_{\text{max}} = 1$, $g \equiv 1$ and the ellipse is fully contained in the patch Ω (the choice of $M_{\text{max}} = 1$ translates into having moments of degree up to 2).

Proof: See Appendix B.

B. Multiple ellipse detection

The detection of N ellipses can be considered as a direct generalization of (9) when the degree of the generating polynomial is $2N$ (multiplying the polynomials associated with each ellipse). However, this approach is likely to fail when there is noise or the ellipses intersect like the one in Fig. 1. Indeed, estimating the shape boundaries based on image moments involves polynomial root finding which is a nonlinear operation. As the degree of the polynomial increases, the nonlinearity order of the overall operation also increases, which causes instability against noise and model mismatch (intersecting ellipses). In this paper, instead of increasing the degree of the polynomial, we propose a patch-wise recovery (detection) algorithm, in which we divide the image into multiple overlapping patches and search for a single ellipse in each patch. To be able to correctly detect an ellipse that is partially observed in a patch, the generalized moments shall be defined locally. More specifically, the weight function $g(\cdot, \cdot)$ should be such that $x^i y^j g(x, y)$, $x^j y^j g_x(x, y)$ and $x^i y^j g_y(x, y)$ all vanish (or approximately vanish) beyond the patch borders for all $i+j \leq 5$. We assume this constraint is fulfilled in the sequel¹.

Our patch-wise approach consists of sliding an $m \times m$ window/patch over the image and evaluating the generalized moments solely based on the pixels within this window. m is chosen such that the mentioned vanishing property of $g(\cdot, \cdot)$

¹In our simulations, for each blurring kernel φ , we numerically find a g that satisfies these constraints.

and its derivatives is fulfilled. Next, we fit a single ellipse to the derived generalized moments by solving (16). If the pixels in the considered window belong to a single ellipse and a sufficient amount of the ellipse's border is contained in the patch, Theorem 3 implies that our recovered ellipse shall coincide with the original one. However, if the window contains an insufficient amount of an ellipse's border, or the window reflects a junction in which pixels represent multiple ellipses, the argument is no longer valid. Therefore, we assign a fidelity value to each fitted ellipse: we form two images composed solely of this ellipse, one with black interior and the other with white interior. Then, we sample these images to regenerate the pixels within the same $m \times m$ window. Let $d_{i,j}$ represent the original pixels within the window, and $e_{i,j}^B$ and $e_{i,j}^W$ denote the pixels of the images of the fitted ellipses with black and white interiors, respectively, within the same window. We initially define the fidelity of black/white ellipse fitting as

$$\begin{aligned} \text{Fidelity}^B &= \rho(d, e^B)\beta(e^B), \\ \text{Fidelity}^W &= \rho(d, e^W)\beta(e^W), \end{aligned} \quad (20)$$

where

$$\rho(d, e) = \frac{\sum_{i,j} d_{i,j} e_{i,j}}{\sqrt{\sum_{i,j} d_{i,j}^2} \sqrt{\sum_{i,j} e_{i,j}^2}} \quad (21)$$

is a measure of correlation (ranging from 0 and 1) between the original pixels and the pixels of the fitted ellipse, and

$$\beta(e) = 2 \sqrt{\frac{(\sum_{i,j} 1_{(e_{i,j} > 0.5)}) (\sum_{i,j} 1_{(e_{i,j} < 0.5)})}{m^2}} \quad (22)$$

roughly describes what fraction of the pixels in the image of the fitted ellipse represent the shape border. Next, we define the overall fidelity of the window/patch as

$$\text{Fidelity}(\text{window}) = \max(\text{Fidelity}^B, \text{Fidelity}^W). \quad (23)$$

In addition, we assign the label B or W to each window depending on whether the ellipse with the black interior had a higher fidelity value or the white one.

At the end of the sliding procedure, we have many fitted ellipses accompanied with fidelity values and B/W labels. However, it is likely that an ellipse is detected in multiple windows (Fig. 2-b). Therefore, we need to unify/merge such ellipses. For this purpose, we construct a merge-graph consisting of all the patches (or ellipses) as the vertices. Our goal is to connect vertices that represent the same ellipse and identify each connected component of the graph as a single ellipse. For instance, Fig. 2-b shows the subgraph for 10 patches and the 3 connected components each representing an ellipse. The connections in the merge-graph are formed as below: if the B/W labels of the ellipses corresponding to the i th and j th patches are different, their vertices are not connected. If the labels are the same, we consider the set of pixels of the corresponding ellipses over the full image (not restricted to the patches), and denote them by E_i and E_j , respectively. Let $E_{i|i}$ and $E_{i|j}$ (similarly, $E_{j|i}$ and $E_{j|j}$) be the subset of pixels of E_i (similarly, E_j) restricted to the i th and j th patches, respectively. If any of the correlations $\rho(E_{i|i}, E_{j|i})$ and $\rho(E_{i|j}, E_{j|j})$ exceeds a predefined threshold T_m (we use

the default value 0.95), where ρ is the same as in (21), then, we connect the associated vertices in the merge-graph. After all pairs of ellipses are checked, we fit a single ellipse to each connected component of the merge-graph that best describes all the generalized moments within the connected patches. We highlight that the connected components are not necessarily complete graphs. Moreover, we define the fidelity value of the fitted ellipse as the sum of all the involved fidelity values. This sum is again roughly proportional to the length of the perimeter of the ellipse that is correctly detected in the whole image. Finally, we discard all the ellipses that have overall fidelity values below another predefined threshold T_f (we use the default value 1).

An important issue in our patch-wise approach is the shift of the origin. The coordinate origin in the annihilation equations of each window is automatically the center of that window. This means that the shift of the coordinates shall be taken into account for comparing the ellipse coefficients (see Fig. 2). By convention, we set the reference coordinate as the symmetry axes of the image plane. Thus, by sliding the window, the coordinate is shifted by (x_0, y_0) and the polynomial $p(x, y) = \sum a_{i,j} x^i y^j$ in the reference system shall be mapped to

$$\begin{aligned} \bar{p}(x, y) &= p(x + x_0, y + y_0) \\ &= \sum_{0 \leq i, j, i+j \leq 2} a_{i,j} (x + x_0)^i (y + y_0)^j \\ &= \sum_{0 \leq i, j, i+j \leq 2} a_{i,j} \sum_{k=0}^i \sum_{l=0}^j \binom{i}{k} x_0^{i-k} \binom{j}{l} y_0^{j-l} x^k y^l \\ &= \sum_{0 \leq k, l, k+l \leq 2} b_{k,l} x^k y^l, \end{aligned}$$

where

$$b_{k,l} = \sum_{\substack{k \leq i, l \leq j \\ i+j \leq 2}} \binom{i}{k} \binom{j}{l} x_0^{i-k} y_0^{j-l} a_{i,j}, \quad (24)$$

This can be written in the matrix form as

$$\mathbf{b} = \mathbf{B}^{(x_0, y_0)} \mathbf{a}, \quad (25)$$

where

$$\mathbf{B}^{(x_0, y_0)} = \begin{bmatrix} 1 & y_0 & x_0 & y_0^2 & x_0 y_0 & x_0^2 \\ 0 & 1 & 0 & 2y_0 & x_0 & 0 \\ 0 & 0 & 1 & 0 & y_0 & 2x_0 \\ 0 & 0 & 0 & 1 & 0 & 0 \\ 0 & 0 & 0 & 0 & 1 & 0 \\ 0 & 0 & 0 & 0 & 0 & 1 \end{bmatrix} \quad (26)$$

is an invertible upper-triangular matrix. Now if $\mathbf{M}_{(x_0, y_0)}$ denotes the matrix of generalized moments of the window with center (x_0, y_0) , the annihilation equations in the local coordinate system can be rewritten in the global coordinates as

$$\mathbf{M}_{(x_0, y_0)} \mathbf{b} = \underbrace{\mathbf{M}_{(x_0, y_0)} \mathbf{B}^{(x_0, y_0)}}_{\text{Global annihilation filter}} \mathbf{a} = \mathbf{0}. \quad (27)$$

In summary, we update the moment matrix $\mathbf{M}_{(x_0, y_0)}$ of each window with the associated multiplier $\mathbf{B}^{(x_0, y_0)}$ before estimating the ellipse coefficients. With this modification, we always achieve the coefficients with respect to the global coordinate

Algorithm 1 Multiple Ellipse Detection

```

1: Input:
2:   Measured pixels  $\{d_{k,l}\}$ 
3:   Merge and fidelity threshold values  $T_m, T_f$ 
4: Output:
5:   Detected ellipses with  $B/W$  labels
6: procedure ELLIPSE DETECTION( $\{d_{k,l}\}, T_m, T_f$ )
7:   for each patch do
8:     Evaluate  $\mathbf{M}_{(x_0,y_0)}$  according to (11)
9:     Fit an ellipse to  $\mathbf{M}_{(x_0,y_0)}$  via (16)
10:    Evaluate Fidelity in (23) and set the  $B/W$  label
11:   end for
12:   Construct the merge-graph with threshold  $T_m$ 
13:   Fit an ellipse to each connected component of the
   merge-graph and define its fidelity value
14:   Discard ellipses with overall fidelity values below  $T_f$ 
15:   return Detected ellipses.
16: end procedure

```

system of the image. These details are also illustrated in Algorithm 1.

IV. SIMULATION RESULTS

In this section, we conduct various experiments to evaluate the performance of the proposed algorithm and compare it against some of the existing techniques such as HT [5], DLS [18], the algebraic curve recovery in [1], and a widely used ImageJ plugin for ellipse recovery [37].

In our first experiment, we consider the recovery of a single ellipse from blurred noiseless and noisy pixels. Figure 3(a) depicts the original image of size 3001×3001 (in pixels), which is blurred with the 2D B-spline kernel of degree 2 with a support of 300 pixels and uniformly sub-sampled to form the 33×33 pixel image in Fig. 3(b). The noisy pixels in Fig. 3(c) are found by adding Gaussian noise with $\text{SNR} = 5\text{dB}$ to the noiseless pixels in Fig. 3(b). Besides the proposed method, we consider the HT and DLS methods in this experiment. Figures 3(d)-(f) represent the reconstruction error (black pixels indicate perfect recovery) of HT, DLS, and the proposed method respectively. With an PSNR of 52.64dB, the proposed method achieves a remarkably better reconstruction compared to $\text{PSNR} = 21.33\text{dB}$ for HT and $\text{PSNR} = 21.70\text{dB}$ for DLS. The same pattern is also observed in the reconstruction under noise shown in Fig. 3(g)-(i); $\text{PSNR} = 24.87\text{dB}$ for the proposed method compared to $\text{PSNR} = 12.02\text{dB}$ for HT and $\text{PSNR} = 4.90\text{dB}$ for DLS. To further investigate the performances under noise, we have plotted Fig. 4, where for each input SNR value, the resulting PSNR values are averaged over 200 realizations.

Unlike the HT and DLS methods, the algebraic technique in [1] is able to incorporate the blurring kernel in the reconstruction. However, this approach models the whole image as a single algebraic shape. To better illustrate the drawback of this approach, we have considered a 4201×4201 -pixel image with 5 ellipses in Fig. 5-(a). The 49×49 blurred pixels in Fig. 5-(b) were the result of a B-spline kernel of degree 6 with a support

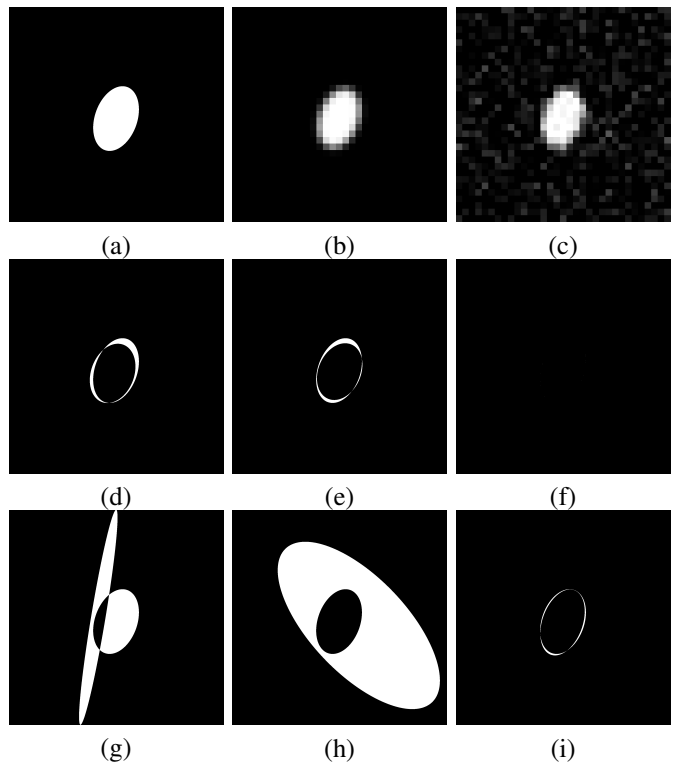


Fig. 3. Ellipse recovery in noiseless and noisy scenarios from blurred pixels. (a) The input image with size 3001×3001 , (b) noiseless samples of size 33×33 , (c) noisy samples with $\text{SNR} = 5\text{dB}$. The reconstruction error with noiseless samples using the HT method (d), DLS method (e), and the proposed method (f) achieve PSNR values of 21.33dB, 21.70dB, and 52.64dB, respectively. The reconstruction error with noisy samples using the HT method (g), DLS method (h), and the proposed method (i) achieve PSNR values of 12.02dB, 4.90dB, and 24.87dB, respectively.

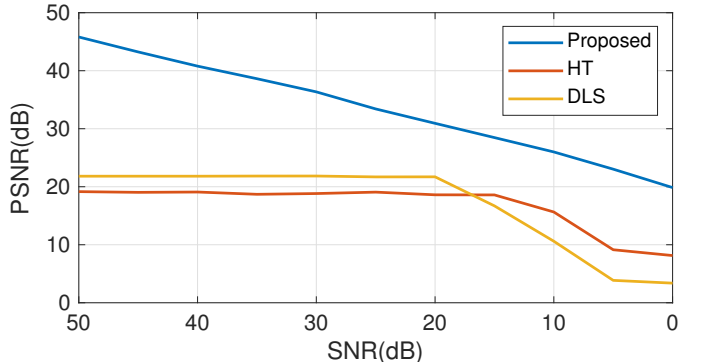


Fig. 4. Effect of noise on the recovery of the ellipse in 3(a) from blurred pixels.

of 700 pixels. The reconstruction error of the proposed method depicted in Fig. 5-(c) amounts to PSNR values of 27.97dB.

In our next experiment, we consider the 5801×5801 -pixels image in Fig. 6-(a) that contains ellipses with both black and white interiors. The blurred image in Fig. 6-(b) is of size 65×65 for which a B-spline of degree 6 with the support of 700 pixels is used. The reconstruction errors using the method of [1] (with $\text{PSNR} = 12.38\text{dB}$) and the proposed method (with $\text{PSNR} = 26.25\text{dB}$) are shown in Fig. 6-(c) and 6-(d), respectively.

We now compare our method with the ImageJ ellipse split software of [37]. For this purpose, we consider the original image of size 3001×3001 in Fig. 7-(a) which is

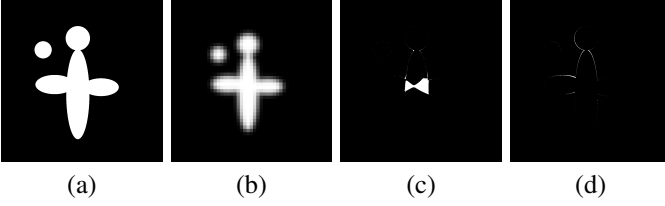


Fig. 5. Recovery of multiple intersecting ellipses. (a) The original image of size 4201×4201 pixels, (b) the blurred image of size 49×49 , (c) the reconstruction error of [1] (PSNR = 20.82dB), and (d) the reconstruction error of the proposed algorithm (PSNR = 27.97dB).

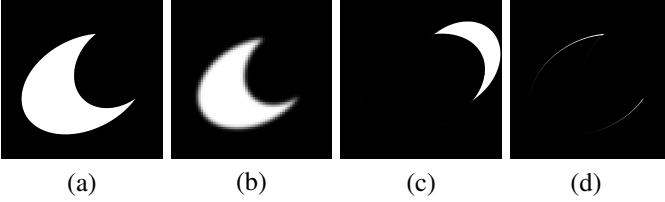


Fig. 6. (a) The original image with size 5801×5801 pixels, (b) 65×65 blurred image, (c) the error of recovering a polynomial of degree 4 with the method of [1] (PSNR = 12.38 dB), and (d) the reconstruction error (PSNR = 26.25 dB).

sampled as a 37×37 -pixel image after being blurred by a B-spline kernel of degree 6 with the support of 700 pixels (Fig. 7-(b)). The proposed method recovers this image with PSNR = 34.12dB (the reconstruction error is shown in Fig. 7-(c)). The ImageJ plugin can only work with binary-valued input pixels (black/white), while the pixels in Fig. 7-(b) are gray-level due to the blurring kernel. For this purpose, we threshold the gray-level image to obtain a black and white image; to avoid dependence on the threshold value, we apply all threshold values from 0.1 to 0.9 with the step size of 0.1 in Fig. 8. The detected ellipses of the software are also drawn on top of each image in Fig. 8. It is evident that the software was never able to detect the number of ellipses correctly, which is justifiable (the software is unaware of the PSF).

In the next experiment, we examine the sensitivity of the proposed method to non-ideality of the ellipse shapes. For this purpose, we consider red blood cells, which are fairly approximated with ellipse shapes. Figure 9-(a) taken from the open library [38], depicts the original gray-level image of blood-cells. We first threshold this image to achieve a 5001×5001 binary image consisting of multiple roughly-ellipse shapes. We blur the resulting image with a B-spline kernel of degree 6 with the support of 700 pixels, and subsample it to obtain a 57×57 image (Fig. 9-(b)). By applying the proposed method on the latter image, we obtain Fig. 9-(c) which consists of exact ellipses; the difference between the reconstructed image and the original binary image is shown in Fig. 9-(d), which is measured as PSNR = 15.93dB.

In the last experiment, we use a microscopy image of human HT29 cells taken from [39]. As we do not have access to the imaging device, we are unaware of the blurring kernel a priori. To proceed, we have assumed the kernel to be Gaussian (a fair assumption in many cases) and estimated the variance as $\sigma = 0.8$ based on the thickness of the edges in terms of the number of pixels. With setting the sampling period $\hat{T} = 50$ (the desired magnification ratio), the result in Fig. 10-(c) is obtained. For verifying the assumption, we have regenerated

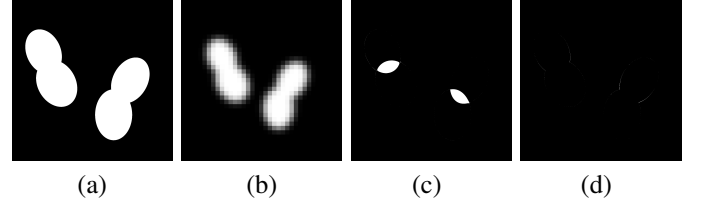


Fig. 7. Two pairs of intersecting ellipses. (a) The original image with size 3001×3001 (b) the blurred image of size 37×37 , (c) reconstruction error of [1] (PSNR = 18.42dB), and (d) the reconstruction error of the proposed method (PSNR = 34.21dB).

the blurred and down-sampled image in Fig. 10-(d). While the shapes in Fig. 10-(b) and Fig. 10-(d) are not exactly the same, the estimated ellipses are acceptable approximations.

V. CONCLUSION

In this paper, we focused on recovery elliptical shapes from pixels. We design a sampling and reconstruction algorithm for elliptical binary shapes where they are the zero level of a bivariate polynomial. We derived a set of linear annihilation equations from the pixels and proved that the ellipse boundary is the solution of this system. We improved the degree of moments for exact recovery in the case ellipse and decreases the previous bounds. Also, to make algorithm stable to noise, we aid generalized moments instead conventional moments. We showed that from a patch of pixel, the ellipse can be recovered. For the case of multiple ellipses, we proposed a patch based algorithm that recover every ellipse from a patch. Hence, instead of estimating a polynomial of high degree, we always recover a polynomial of degree 2 which increases the robustness of the algorithm against noise.

APPENDIX

A. Proof of Theorem 2

Using the Lagrange multipliers we know that the minimizer of (16) shall satisfy

$$\mathbf{M}^T \mathbf{M} \mathbf{a}_{\text{opt}} = \lambda \mathbf{C} \mathbf{a}_{\text{opt}}, \quad (28)$$

$$\mathbf{a}_{\text{opt}}^T \mathbf{C} \mathbf{a}_{\text{opt}} = 1, \quad (29)$$

for some suitable scalar λ . The first equation presents a general eigen-value problem. If we multiply both sides of the first equation by $\mathbf{a}_{\text{opt}}^T$, we have that

$$\mathbf{a}_{\text{opt}}^T \mathbf{M}^T \mathbf{M} \mathbf{a}_{\text{opt}} = \lambda \mathbf{a}_{\text{opt}}^T \mathbf{C} \mathbf{a}_{\text{opt}} = \lambda. \quad (30)$$

Since \mathbf{M} is full column-rank, $\mathbf{M}^T \mathbf{M}$ is strictly positive-definite and $0 < \mathbf{a}_{\text{opt}}^T \mathbf{M}^T \mathbf{M} \mathbf{a}_{\text{opt}}$. Therefore, λ shall be strictly positive. In addition, if $\mathbf{Q} = \sqrt{\mathbf{M}^T \mathbf{M}}$, we can rewrite (28) as

$$\frac{1}{\lambda} (\mathbf{Q} \mathbf{a}_{\text{opt}}) = (\mathbf{Q}^{-1} \mathbf{C} \mathbf{Q}^{-1}) (\mathbf{Q} \mathbf{a}_{\text{opt}}). \quad (31)$$

Thus, $\mathbf{Q} \mathbf{a}_{\text{opt}}$ is an eigen-vector of $\mathbf{Q}^{-1} \mathbf{C} \mathbf{Q}^{-1}$ with eigen-value $\frac{1}{\lambda}$. It is known that the sign of the eigen-values of $\mathbf{Q}^{-1} \mathbf{C} \mathbf{Q}^{-1}$ and \mathbf{C} are the same [40]; hence, $\mathbf{Q}^{-1} \mathbf{C} \mathbf{Q}^{-1}$ has only one positive eigen-value (the eigen-values of \mathbf{C} are $\{2, 0, 0, -1, -2\}$). Consequently, $\mathbf{Q} \mathbf{a}_{\text{opt}}$ is the eigen-vector of $\mathbf{Q}^{-1} \mathbf{C} \mathbf{Q}^{-1}$ corresponding to the maximum eigen-value (which is unique). It is straightforward to complete the proof of the theorem by considering (29). ■

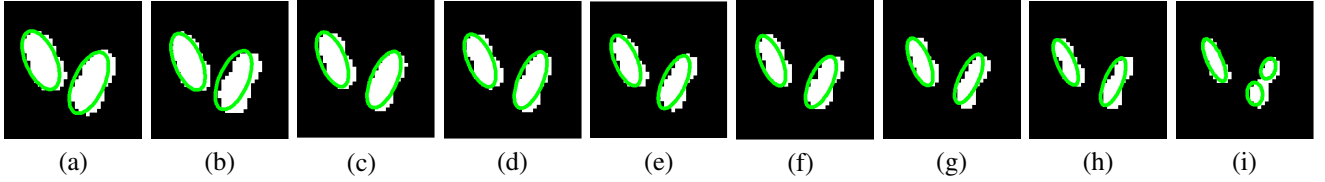


Fig. 8. The results of the ImageJ ellipse split package [37] applied to the thresholded 37×37 blurred image in Fig. 7(b) using threshold values 0.1 to 0.9 with the step size of 0.1 (subfigures (a) to (i)).

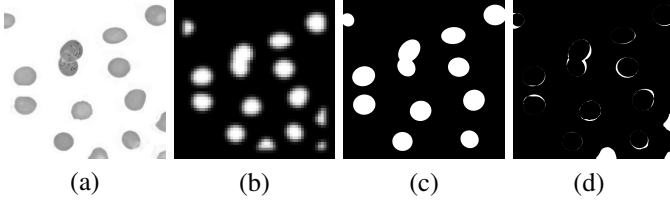


Fig. 9. (a) The original image of blood cells, (b) the pixelized data, (c) the recovered image, and (d) the reconstruction error.

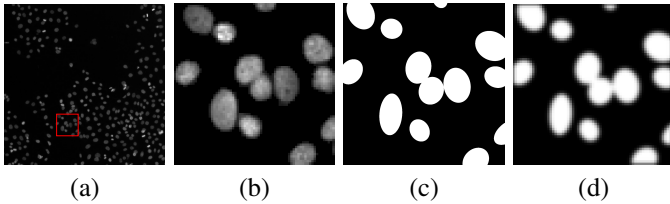


Fig. 10. (a) The available microscopy image, (b) a part of the image with size (65×65) pixels, (c) reconstructed image (1201×1201) pixels assuming a Gaussian blurring kernel with variance $(\sigma = 0.8)$ and sampling period of $\hat{T} = 50$ pixels, and (d) the pixelized version of the reconstructed image.

B. Proof of Theorem 3

Let $I(x, y)$ represent an arbitrary ellipse associated with $p(x, y) = \sum a_{i,j} x^i y^j$. Here, we prove part (b) of the claim, as part (a) is obtained from Theorem 1 by setting $n = 2$. Therefore, we assume $g \equiv 1$ and $g_x = g_y \equiv 0$. We first show that by having the moments of $I(x, y)$, we can obtain the moments of rotated, scaled and translated versions of $I(x, y)$. For this purpose, let $\Gamma = [\gamma_{i,j}]_{2 \times 2}$ with $\det(\Gamma) > 0$ be an invertible matrix with inverse $\Lambda = [\lambda_{i,j}]_{2 \times 2} = \Gamma^{-1}$ and $\det(\Lambda) = d_\Lambda$. We define

$$J(x, y) \triangleq I(\gamma_{1,1}x + \gamma_{1,2}y + \xi_1, \gamma_{2,1}x + \gamma_{2,2}y + \xi_2),$$

where ξ_1, ξ_2 are real numbers. Indeed, $J(x, y)$ represents a rotated, scaled and translated version of $I(x, y)$; alternatively, any rotated, scaled and translated version of $I(x, y)$ could be represented in this form. We assume $\gamma_{i,j}$ s and ξ_i s are such that the ellipse $J(x, y)$ is also fully contained in Ω . For the moments of $J(x, y)$ we have that

$$\begin{aligned} & \iint_{\Omega} x^i y^j J(x, y) dx dy \\ &= \iint_{\Omega} x^i y^j I(\underbrace{\gamma_{1,1}x + \gamma_{1,2}y + \xi_1}_X, \underbrace{\gamma_{2,1}x + \gamma_{2,2}y + \xi_2}_Y) dx dy \\ &= \sum_{\substack{i_1+i_2 \leq i \\ i_1, i_2 \geq 0}} \sum_{\substack{j_1+j_2 \leq j \\ j_1, j_2 \geq 0}} C_{j_1, j_2}^{i_1, i_2} \iint X^{i_1+j_1} Y^{i_2+j_2} I(X, Y) dX dY, \end{aligned} \quad (32)$$

where

$$\begin{aligned} C_{j_1, j_2}^{i_1, i_2} &= d_\Lambda \binom{i}{i_1, i_2, i - i_1 - i_2} \binom{j}{j_1, j_2, j - j_1 - j_2} \times \\ & \lambda_{1,1}^{i_1} \lambda_{1,2}^{i_2} \lambda_{2,1}^{j_1} \lambda_{2,2}^{j_2} (-\lambda_{1,1}\xi_1 - \lambda_{1,2}\xi_2)^{i-i_1-i_2} \times \\ & (-\lambda_{2,1}\xi_1 - \lambda_{2,2}\xi_2)^{j-j_1-j_2}. \end{aligned} \quad (33)$$

Therefore, the moments of $J(x, y)$ could be obtained by linear combinations of the moments of $I(x, y)$. In addition, for a fixed and invertible Γ , the mapping from I to J is one-to-one. This implies that reconstructing $J(x, y)$ is equivalent to reconstructing $I(x, y)$. Consequently, if we prove that the moments of $J(x, y)$ uniquely determine $J(x, y)$, we shall have the same statement for $I(x, y)$.

Our approach is to use a matrix Γ such that $J(x, y)$ corresponds to the disk $x^2 + y^2 = r^2$ (where r is small enough that the disk fits within Ω); it is straightforward that this operation could be accomplished by applying a rotation (with respect to the center of Ω) to make the ellipse axes parallel to the coordinate axes, separate downscaling of the horizontal and vertical axes to convert the ellipse into a circle with ratios larger than $\sqrt{2}$ to ensure that the circle is fully contained in Ω , and a translation to center the ellipse inside Ω . Hence, to prove part (b) of Theorem 3, we can now safely assume that $I(x, y)$ is associated with $p(x, y) = x^2 + y^2 - r^2$. It is not difficult to check that the moments of the disk $p(x, y) = x^2 + y^2 - r^2$ are given as

$$\begin{aligned} M_{0,1}^1 &= M_{1,0}^1 = M_{2,1}^1 = M_{1,2}^1 = M_{1,1}^1 = 0, \\ M_{0,0}^1 &= \pi r^2, \quad M_{0,2}^1 = M_{2,0}^1 = \frac{\pi}{4} r^4. \end{aligned} \quad (34)$$

Besides, the matrix \mathbf{M} in this case has the form

$$\begin{aligned} \mathbf{M} &= \begin{bmatrix} 0 & M_{0,0}^1 & 0 & 2M_{1,0}^1 & M_{0,1}^1 & 0 \\ M_{0,0}^1 & 2M_{1,0}^1 & M_{0,1}^1 & 3M_{2,0}^1 & 2M_{1,1}^1 & M_{0,2}^1 \\ 0 & M_{0,1}^1 & 0 & 2M_{1,1}^1 & M_{0,2}^1 & 0 \\ 0 & 0 & M_{0,0}^1 & 0 & M_{1,0}^1 & 2M_{0,1}^1 \\ 0 & 0 & M_{1,0}^1 & 0 & M_{2,0}^1 & 2M_{1,1}^1 \\ M_{0,0}^1 & M_{1,0}^1 & 2M_{0,1}^1 & M_{2,0}^1 & 2M_{1,1}^1 & 3M_{0,2}^1 \end{bmatrix} \\ &= \frac{\pi r^2}{4} \begin{bmatrix} 0 & 4 & 0 & 0 & 0 & 0 \\ 4 & 0 & 0 & 3r^2 & 0 & r^2 \\ 0 & 0 & 0 & 0 & r^2 & 0 \\ 0 & 0 & 4 & 0 & 0 & 0 \\ 0 & 0 & 0 & 0 & r^2 & 0 \\ 4 & 0 & 0 & r^2 & 0 & 3r^2 \end{bmatrix}. \end{aligned} \quad (35)$$

The reduced echelon form for \mathbf{M} is given as

$$\frac{\pi r^2}{4} \begin{bmatrix} 1 & 0 & 0 & 0 & 0 & r^2 \\ 0 & 1 & 0 & 0 & 0 & 0 \\ 0 & 0 & 1 & 0 & 0 & 0 \\ 0 & 0 & 0 & 1 & 0 & -1 \\ 0 & 0 & 0 & 0 & 1 & 0 \\ 0 & 0 & 0 & 0 & 0 & 0 \end{bmatrix}. \quad (36)$$

Therefore, we conclude that $\text{rank}(\mathbf{M}_{6 \times 6}) = 5$, or equivalently, the null-space of \mathbf{M} is one-dimensional. Let $\tilde{p}(x, y) = \sum_{i+j \leq 2} \tilde{a}_{i,j} x^i y^j$ be any solution of (16); thus, $\mathbf{M}\tilde{\mathbf{a}} = \mathbf{0}$, i.e., $\tilde{\mathbf{a}}$ shall be in the null-space of \mathbf{M} . As the null-space of \mathbf{M} is one-dimensional, all possible solutions $\tilde{\mathbf{a}}$ are scaled versions of the particular solution $\mathbf{a} = [-r^2, 0, 0, 1, 0, 1]^T$. Hence, $\tilde{p}(x, y)$ differs from $p(x, y) = x^2 + y^2 - r^2$ only by a scalar constant, which does not change the roots. Consequently, $\tilde{p}(x, y)$ generates the same algebraic shape. ■

REFERENCES

- [1] M. Fatemi, A. Amini, and M. Vetterli, "Sampling and reconstruction of shapes with algebraic boundaries," *IEEE Transactions on Signal Processing*, vol. 64, no. 22, pp. 5807–5818, Nov 2016.
- [2] G. Farin, *Curves and Surfaces for Computer-Aided Geometric Design (Third Edition)*, third edition ed. Boston: Academic Press, 1993.
- [3] L. d. F. D. Costa and R. M. Cesar, Jr., *Shape Analysis and Classification: Theory and Practice*, 1st ed. CRC Press, Inc., 2000.
- [4] T.-C. Chen and K.-L. Chung, "An efficient randomized algorithm for detecting circles," *Computer Vision and Image Understanding*, vol. 83, no. 2, pp. 172 – 191, 2001.
- [5] X. Bai, C. Sun, and F. Zhou, "Splitting touching cells based on concave points and ellipse fitting," *Pattern Recognition*, vol. 42, no. 11, pp. 2434 – 2446, 2009.
- [6] N. Ray, "A concave cost formulation for parametric curve fitting: Detection of leukocytes from intravital microscopy images," in *IEEE International Conference on Image Processing*, Sep 2010, pp. 53–56.
- [7] I. N. Bankman, *Handbook of medical imaging processing and analysis*, 2000.
- [8] R. Delgado-Gonzalo, P. Thevenaz, C. S. Seelamantula, and M. Unser, "Snakes with an ellipse-reproducing property," *Trans. Img. Proc.*, vol. 21, no. 3, pp. 1258–1271, Mar. 2012.
- [9] D. Liu and J. Liang, "A Bayesian approach to diameter estimation in the diameter control system of silicon single crystal growth," *IEEE Transactions on Instrumentation and Measurement*, vol. 60, no. 4, pp. 1307–1315, Apr 2011.
- [10] A. Soetedjo.
- [11] E. T. M. W. Christian Teutsch, Dirk Berndt, "Real-time detection of elliptic shapes for automated object recognition and object tracking," 2006.
- [12] L. Świrski, A. Bulling, and N. Dodgson, "Robust real-time pupil tracking in highly off-axis images," in *Proceedings of the Symposium on Eye Tracking Research and Applications*, ser. ETRA '12. New York, NY, USA: ACM, 2012, pp. 173–176.
- [13] V. F. Leavers, *Shape Detection in Computer Vision Using the Hough Transform*. Berlin, Heidelberg: Springer-Verlag, 1992.
- [14] N. Guil and E. Zapata, "Lower order circle and ellipse Hough transform," *Pattern Recognition*, vol. 30, no. 10, pp. 1729 – 1744, 1997.
- [15] S.-C. Zhang and Z.-Q. Liu, "A robust, real-time ellipse detector," *Pattern Recognition*, vol. 38, no. 2, pp. 273 – 287, 2005.
- [16] Y. Xie and Q. Ji, "A new efficient ellipse detection method," in *Object recognition supported by user interaction for service robots*, vol. 2, Aug 2002, pp. 957–960 vol.2.
- [17] F. L. Bookstein, "Fitting conic sections to scattered data," *Computer Graphics and Image Processing*, vol. 9, no. 1, pp. 56 – 71, 1979.
- [18] A. Fitzgibbon, M. Pilu, and R. B. Fisher, "Direct least square fitting of ellipses," *IEEE Transactions on Pattern Analysis and Machine Intelligence*, vol. 21, no. 5, pp. 476–480, May 1999.
- [19] R. Halir and J. Flusser, "Numerically stable direct least squares fitting of ellipses," 1998.
- [20] S. J. Ahn, W. Rauh, and H.-J. Warnecke, "Least-squares orthogonal distances fitting of circle, sphere, ellipse, hyperbola, and parabola," *Pattern Recognition*, vol. 34, no. 12, pp. 2283 – 2303, 2001.
- [21] S. J. Ahn, W. Rauh, H. S. Cho, and H.-J. Warnecke, "Orthogonal distance fitting of implicit curves and surfaces," *IEEE Transactions on Pattern Analysis and Machine Intelligence*, vol. 24, no. 5, pp. 620–638, 2002.
- [22] M. Vetterli, P. Marziliano, and T. Blu, "Sampling signals with finite rate of innovation," *IEEE Transactions on Signal Processing*, vol. 50, no. 6, pp. 1417–1428, Jun 2002.
- [23] I. Maravic and M. Vetterli, "Exact sampling results for some classes of parametric nonbandlimited 2-d signals," *IEEE Transactions on Signal Processing*, vol. 52, no. 1, pp. 175–189, Jan 2004.
- [24] S. Mulleti and C. S. Seelamantula, "Ellipse fitting using the finite rate of innovation sampling principle," *IEEE Transactions on Image Processing*, vol. 25, no. 3, pp. 1451–1464, March 2016.
- [25] H. Pan, T. Blu, and P. L. Dragotti, "Sampling curves with finite rate of innovation," *IEEE Transactions on Signal Processing*, vol. 62, no. 2, pp. 458–471, Jan 2014.
- [26] M. Fatemi, A. Amini, L. Baboulaz, and M. Vetterli, "Shapes from pixels," *IEEE Transactions on Image Processing*, vol. 25, no. 3, pp. 1193–1206, March 2016.
- [27] G. Ongie and M. Jacob, "Off-the-grid recovery of piecewise constant images from few Fourier samples," *SIAM Journal on Imaging Sciences*, vol. 9, no. 3, pp. 1004–1041, 2016.
- [28] H. M. Dolatabadi and A. Amini, "A sampling theorem for convex shapes with algebraic boundaries," in *2017 International Conference on Sampling Theory and Applications (SampTA)*, Jul 2017, pp. 499–503.
- [29] A. A. Rad, K. Faez, and N. Qaragozlou, "Fast circle detection using gradient pair vectors," in *Proc. VIIIth Digital Image Computing: Techniques and Applications*, 2003.
- [30] H. Jiandong, "Ellipse detection based on principal component analysis," in *2010 International Conference on Computer Application and System Modeling (ICCASM 2010)*, vol. 9, Oct 2010, pp. V9–258–V9–261.
- [31] W. Chojnacki, M. J. Brooks, A. Van Den Hengel, and D. Gawley, "On the fitting of surfaces to data with covariances," *IEEE Transactions on pattern analysis and machine intelligence*, vol. 22, no. 11, pp. 1294–1303, 2000.
- [32] S. B. Hadji, F. Chatelain, X. Descombes, and J. Zerubia, "Parameter estimation for a marked point process within a framework of multi-dimensional shape extraction from remote sensing images," in *ISPRS Conference on Photogrammetry Computer Vision and Image Analysis*, vol. XXXVIII, 2010.
- [33] E. Sobhani, M. Sadeghi, M. Babaie-Zadeh, and C. Jutten, "A robust ellipse fitting algorithm based on sparsity of outliers," in *2017 25th European Signal Processing Conference (EUSIPCO)*. IEEE, 2017, pp. 1195–1199.
- [34] A. Jabbar, A. Mendes, and S. Chalup, "Comparing ellipse detection and deep neural networks for the identification of drinking glasses in images," in *Computer Vision Systems*, D. Tzovaras, D. Giakoumis, M. Vincze, and A. Argyros, Eds. Cham: Springer International Publishing, 2019, pp. 319–329.
- [35] M. Unser, "Splines: a perfect fit for signal and image processing," *IEEE Signal Processing Magazine*, vol. 16, no. 6, pp. 22–38, Nov 1999.
- [36] P. L. Dragotti, M. Vetterli, and T. Blu, "Sampling moments and reconstructing signals of finite rate of innovation: Shannon meets Strang-Fix," *IEEE Transactions on Signal Processing*, vol. 55, no. 5, pp. 1741–1757, May 2007.
- [37] T. Wagner and J. Eglinger, "thorstenwagner/ij-ellipsesplit: EllipseSplit 0.6.0 SNAPSHOT," Jul. 2017.
- [38] "Public health image library (phil)," <https://phil.cdc.gov/>.
- [39] C. McQuin, A. Goodman, V. Chernyshev, L. Kametsky, B. A. Cimini, K. W. Karhohs, M. Doan, L. Ding, S. M. Rafelski, D. Thirstrup *et al.*, "Cellprofiler 3.0: Next-generation image processing for biology," *PLoS biology*, vol. 16, no. 7, p. e2005970, 2018.
- [40] J. Wilkinson, *The algebraic eigenvalue problem*, ser. Monographs on numerical analysis. Oxford, 1965.

Hojatollah Zamani received the B.Sc. degree from University of Tehran, Tehran, Iran, in 2013, and the M.Sc. degree from Sharif University of Technology, Tehran, in 2015, where he is currently pursuing the Ph.D. degree in electrical engineering. His current research interests include signal processing and machine learning, especially compressed sensing and imaging systems.

Arash Amini received the B.Sc., M.Sc., and Ph.D. degrees in electrical engineering (communications and signal processing) and the B.Sc. degree in petroleum engineering (reservoir) from the Sharif University of Technology, Tehran, Iran, in 2005, 2007, 2011, and 2005, respectively. He was a Researcher with the École Polytechnique fédérale de Lausanne, Lausanne, Switzerland, from 2011 to 2013, working on statistical approaches toward modeling sparsity in continuous-domain. He joined Sharif University of Technology as an assistant professor in 2013, where he is now an associate professor since 2018. He has served as an associate editor of *IEEE Signal Processing Letters* from 2014 to 2018. His research interests include various topics in statistical signal processing, specially compressed sensing.